Performance of a solar adsorption cooling and desalination system using aluminum fumarate and silica gel

Mahmoud Badawy Elsheniti[1*], Ahmed Rezk[2,3], Mohamed Shaaban[4], Mohamed Roshdy[4], Yahia Mohamed Nagib[4], Osama. A. Elsamni[4], Bidyut Baran Saha[5,6]

[1]Mechanical Engineering Department, College of Engineering, King Saud University, Riyadh 11451, KSA

[2]Energy and Bioproducts Research Institute (EBRI), College of Engineering and Physical Science, Aston University, Birmingham, UK, B4 7ET

[3]Aston Institute of Material Research (AIMR), College of Engineering and Physical Science, Aston University, Birmingham, UK, B4 7ET

[4]Mechanical Engineering Department, Faculty of Engineering, Alexandria University, Alexandria 21544, Egypt

[5]International Institute for Carbon-Neutral Energy Research (WPI-I2CNER), Kyushu University, 744 Motooka, Nishi-ku, Fukuoka-shi, Fukuoka 819-0395, Japan

[6]Mechanical Engineering Department, Kyushu University, 744 Motooka, Nishi-ku, Fukuoka-shi, Fukuoka 819-0395, Japan

*Corresponding author: Mahmoud Elsayed Badawy Elsheniti, Tel +966557134690

melsheniti@gmail; mbadawy.c@ksu.edu.sa

Abstract

This paper numerically investigated the influence of adsorbent materials' thermal and adsorption characteristics on the overall performance of solar adsorption cooling cum desalination systems. A case study using an array of solar collectors was conducted to compare the emerging Aluminum Fumarate metal-organic framework (Al-Fum) with conventional silica gel (SG) under typical meteorological data at a selected site. Although the adsorption characteristics of Al-Fum outperforms SG at the material level, the former's low thermal characteristics increased the cumulative heat stored and limited the integrated-system performance. The low thermal diffusivity of Al-Fum slowed down the integrated system's response, providing that the average solar COPs of the SG-based system over different months were higher by 83%, 43%, and 22% at inlet chilled water temperatures of 15 °C, 20 °C, and 25 °C, respectively, and 1 mm fin spacing. However, the best specific cooling power of the AF-based system were higher than those of the SG-based system by −16.6%, 16.8%, and 30.5% at these temperatures. Furthermore, the SG-based system was more negatively affected by reducing the heat storage initial temperature from 70 °C to 50 °C, but it attained COP and solar COP higher than those of the AF-based system by 14.9%–63%, respectively.

Keywords: adsorption chiller; desalination; aluminum fumarate; solar cooling; silica-gel.

Highlights

- Aluminum Fumarate is evaluated in a solar hybrid cooling and desalination system.
- The comparison with silica gel spotlights the net effects of a dynamic heat source.
- Interrelated effects of thermal and adsorption characteristics are critical issues.
- Aluminum Fumarate performance is affected negatively by the cumulative heat stored.
- Silica gel system is more responsive to changes in the initial heating temperature.

A_{sc}	Collector aperture area *(m^2)*	$K_S a_v$	Overall mass transfer coefficient (s^{-1})
A_s	One-third of surface area of cylindrical storage tank *(m^2)*	LMTD	Log mean temperature difference (K)
A_1	Coefficient in adsorption isotherms Eq. ($Kg\ Kg^{-1}K^{-1}$)	M	Mass (kg)
A_2	Coefficient in adsorption isotherms Eq. ($Kg\ Kg^{-1}K^{-2}$)	P	Saturated pressure (kPa)
A_3	Coefficient in adsorption isotherms Eq.($Kg\ Kg^{-1}K^{-3}$)	Ru	Universal gas constant ($J\ mol^{-1}K^{-1}$)
A_0	Coefficient in adsorption isotherms Eq. ($Kg\ Kg^{-1}$)	R_p	Particle radius (m)
B_1	Coefficient in adsorption isotherms Eq. (K^{-1})	R_{bm}	Coefficient in total solar irradiance Eq. ($-$)
B_2	Coefficient in adsorption isotherms Eq. (K^{-2})	SCP	Specific cooling Power (WKg^{-1})
B_3	Coefficient in adsorption isotherms Eq. (K^{-3})	SDWP	Specific daily water production ($kg_w\ Kg_{ads}^{-1}\ day^{-1}$)
B_0	Coefficient in adsorption isotherms Eq. (K)	T	Temperature (K)
COP	Coefficient of performance ($-$)	T_{S1}	Top temperature zone of storage tank (K)
c_p	Specific heat ($J\ Kg^{-1}K^{-1}$)	T_{S2}	Intermediate temperature zone of storage tank (K)
D_s	Surface diffusivity ($m^2\ s^{-1}$)	T_{S1}	Low temperature zone of storage tank (K)
D_{so}	Pre-exponential constant ($m^2\ s^{-1}$)	t	Time (sec)
dT/dt	Temperature gradient with time (Ks^{-1})	UA	Overall conductance (WK^{-1})

E_a	Activation energy ($(Jmol^{-1})$	w	Uptake value ($kg_{ref}\ Kg_{ads}^{-1}$)
h	Specific enthalpy ($J\ Kg^{-1}K^{-1}$)	W	Equilibrium uptake ($kg_{ref}\ Kg_{ads}^{-1}$)
I_t	Total solar irradiance ($W\ m^{-2}$)	W_0	Maximum uptake ($kg_{ref}\ Kg_{ads}^{-1}$)
I_b	Beam solar irradiance ($W\ m^{-2}$)		
I_d	Diffuse solar irradiance ($W\ m^{-2}$)		

Subscripts and superscripts:

ads	Adsorbent
bed	Bed
chw	Chilled water
cond	Condenser
cw	Cooling water
evap	Evaporator
f	Fin
g	Gas
Hex	Heat exchanger
HS	Heat storge
hw	Hot water
in	Inlet
out	Outlet
l	Liquid
lg	Liquid-gas
ref	Refrigerant
sat	Saturation
sc	Solar collector
met	Metal
t	Tube
w	Water

Greek symbols:

ΔH_{ads}	Isosteric heat of adsorption (J kg^{-1})
β	Collector slope (°)
ρ	Coefficient in total solar irradiance Eq. $(-)$
η_{col}	Efficiency of collector $(-)$
∂	Flag in Eqs. (1-3)
φ	Flag in Eq. (4)

1 Introduction

With the growth of the world population, the energy consumed to meet the cooling demand in different sectors has been increasing rapidly; this adversely impacts the carbon footprint, primarily due to the use of energy-intensive systems [1, 2]. Additionally, the scarcity of freshwater, which is linked to climate change, has led to different technologies to produce clean water from other resources, such as underground brackish water and seawater [3]. The current technologies for cooling and water desalination are highly energy-intensive; thus, such systems are being decoupled from power grids by integrating renewable energy resources, such as wind and/or solar photovoltaics (PV) [4-6]. Conventional cooling and desalination systems have a high throughput, but the energy conversion efficiency of wind and solar PV systems and the thermal management of electric batteries remain challenging and require considerable capital investment [7-10]. Therefore, the direct utilization of solar thermal energy integrated with heat-driven cooling and/or water desalination systems is a practical alternative, particularly in hot climates [11, 12].

Owing to the unique capability of adsorption cooling and desalination systems to utilize low-grade heat, they are the most feasible energy-efficient heat-driven systems via solar thermal energy [13, 14]. According to the experimental trials by Kim et al.[15], adsorption systems can produce a high quality of freshwater and a byproduct of cooling that is highly beneficial for hot geographical regions. Accordingly, there has been an increasing interest in investigating the development of different packages that employ adsorption cooling or/cum water desalination integrated with solar thermal systems [16]. Sha et al. [17] investigated the performance of small-scale solar-driven activated carbon/methanol adsorption cooling systems through mathematical modelling with emphasis on comparing isothermal and isobaric adsorption physical reaction on the overall system performance. Liu et al. [18] undertook an experimental study investigating the influence of the operating conditions on the performance of solar-driven adsorption cooling system employed SAPO-34 zeolite/water and benchmarked it against silica gel/water working pair. Rezk et al. [19] numerically optimized the operation of a solar-driven adsorption system for hybrid cooling and desalination utilizing silica gel adsorbent by employing a radial movement optimizer coupled with a lumped mathematical model for a system. Logesh et al. [20] qualitatively investigated the influence of mass recovery and operating temperatures in condenser and evaporator on the desalination and cooling throughputs for a solar-driven adsorption system that utilizes silica gel adsorbent. Raj and Baiju [21] emphasized on investigating the effect of the operating temperature on the energy conversion efficiency of solar-driven systems for cooling and desalination through mathematical modeling. With more emphasis on solar energy harnessing, Du et al. [22] optimized the solar thermal collector area aiming at the lowest cost of freshwater production.

Among the wide variety of modeling approaches such as lumped-parameter [23, 24], lumped analytical [25, 26], dynamic [27, 28], distributed parameters [29, 30] and modern 2D & 3D modelling [31, 32],

lumped dynamic modeling is generally appropriate for analyzing the performance at the system and integrated system levels. It is computationally affordable and capable of imitating the intermittent operation of adsorption/desorption processes in adsorption beds and their integration with other components. Lumped dynamic modeling can examine the impact of different working adsorption pairs and their effect on overall system performance. Therefore, it has been adopted to investigate the performance of solar thermal-driven adsorption cooling systems and their interfaces [33-35]. Additionally, lumped dynamic modeling has been used to analyze the performance of solar thermal-driven hybrid adsorption cooling and desalination systems under different climatic conditions [19, 36, 37]. The capability of this modeling approach was extended to develop the empirical lumped analytical model (ELAM), which includes the detailed modeling of adsorption beds by employing the fundamental governing heat and mass transfer equations and the necessary empirical heat transfer correlations of the adsorption system's components as previously detailed by Rezk et al. [38, 39].

The adsorbent material controls the uptake capacity and rate of the adsorbed/desorbed adsorbate and thus the overall energy conversion efficiency of the adsorption systems. Among the available adsorbent materials, metal-organic frameworks (MOFs) showed unique water adsorption characteristics, high porosity, and tunable molecular structures [40, 41]. Over the last two decades, nearly 6000 MOF topologies have been developed, each of which has its own merits [42]. In comparison with conventional adsorbent materials (e.g., silica gel (SG) and zeolites), MOFs are less hydrophilic and thus can release more water vapor at any given operating pressure [43].

Aluminum Fumarate MOF (Al-Fum) has demonstrated outstanding hydrothermal stability alongside its high affinity towards water vapor among the developed MOF topologies. It led to an increasing interest in investigating it for various water adsorption applications. Teo et al. [44-46] experimentally measured the characteristics of Al-Fum for water adsorption and investigated its modulation using formic acid, aiming for better water uptake/offtake performance for cooling applications. With a specific emphasis on water desalination cum cooling, Elsayed et al. [41, 47, 48] measured the characteristics of Al-Fum and benchmarked it against other MOFs, including its influence on water desalination and cooling throughputs. Al-Fum was also used as a reagent to develop adsorption composites of advanced characteristics. Jahan et al. [49] developed an adsorption composite by doping Cobalt with Al-Fum to enhance its thermophysical characteristics.

Building on the improvement of Al-Fum at the material level, its efficient utilization at the component level has been recently investigated. Kummer et al. [50] investigated the spray coating of Al-Fum on a full-scale adsorption reactor, and Tan et al. [51] investigated the in-situ synthesis of Al-Fum monoliths for dehumidification, which showed excellent mechanical stability under typical operating conditions and advanced adsorption kinetics. Saleh et al. [52] numerically and experimentally investigated the packing of Al-Fum into wire-finned and rectangular-finned microchannel heat exchangers, where the former reactor demonstrated a relatively better thermal performance. Nevertheless, the poor thermal

characteristics of MOFs remain an impediment and adversely affect the overall thermal agility of adsorption systems despite their excellent adsorption characteristics [53, 54]. Accordingly, the use of MOF adsorbents in solar thermal-driven adsorption systems remains questionable due to the instability of heat sources and the intermittency of adsorption cycles.

The use of different MOFs in adsorption cooling and/or water desalination systems has been widely investigated. However, there has been little analysis of the contradicting adsorption and thermal characteristics of MOFs and their impact on the overall performance of solar thermal-driven adsorption systems. Therefore, this study compared the overall performance of a solar thermal-driven adsorption system for hybrid cooling and desalination that uses aluminum fumarate (Al-Fum) with the performance of a system that uses a conventional regular density (RD) SG adsorbent. This study was designed to determine whether adsorbent materials of advanced adsorption characteristics enhance energy utilization at the integrated system level. ELAM was employed to predict the performance of a two-bed adsorption system for cooling and desalination that was integrated with evacuated tube solar collectors and hot water heat storage. Typical weather data between April and October for a selected cite (Alexandria, Egypt) were used. To the best of the authors' knowledge, no single study exists which integrates such a detailed numerical model to understand the interrelated effects of the thermal and adsorption characteristics on the overall performance of solar-driven Al-Fum and SG-based systems.

2 System description

As shown in Fig. 1, the studied system consists of three subsystems: evacuated tube solar thermal collectors, hot water tank thermal energy storage, and the adsorption system. The target capacity in the mid of summer season was about 15 kW cooling capacity from about 100 kg adsorbent material; accordingly, the solar collector system comprises 27 evacuated tube units arranged in nine parallel paths (three units in each path) was used to supply about 25 kW heating power. Each unit includes 15 evacuated tubes and has a 1.95 m^2 effective surface area. The intermittency of solar thermal energy is buffered using the hot water tank thermal energy storage. Water leaves the tank from the high-temperature zone at the top point and returns to the tank via the low-temperature zone at the bottom.

The adsorption subsystem consists of two adsorbent beds; each is interconnected to the evaporator in adsorption mode or the condenser in desorption mode. The system operation in adsorption/desorption and preheating/precooling modes and hot- and cold-water flow control were detailed by Elsheniti et al. [55]. The adsorbent bed is constructed from rectangular aluminum fins and plain copper tubes. The adsorbent particles are packed into the inter-fin and inter-tube gaps. Two adsorbent materials were investigated for cooling and desalination purposes: a conventional adsorbent RD SG and an emerging adsorbent Al-Fum. The operational and geometrical parameters for the basic model are illustrated in Table 1 and Table 2

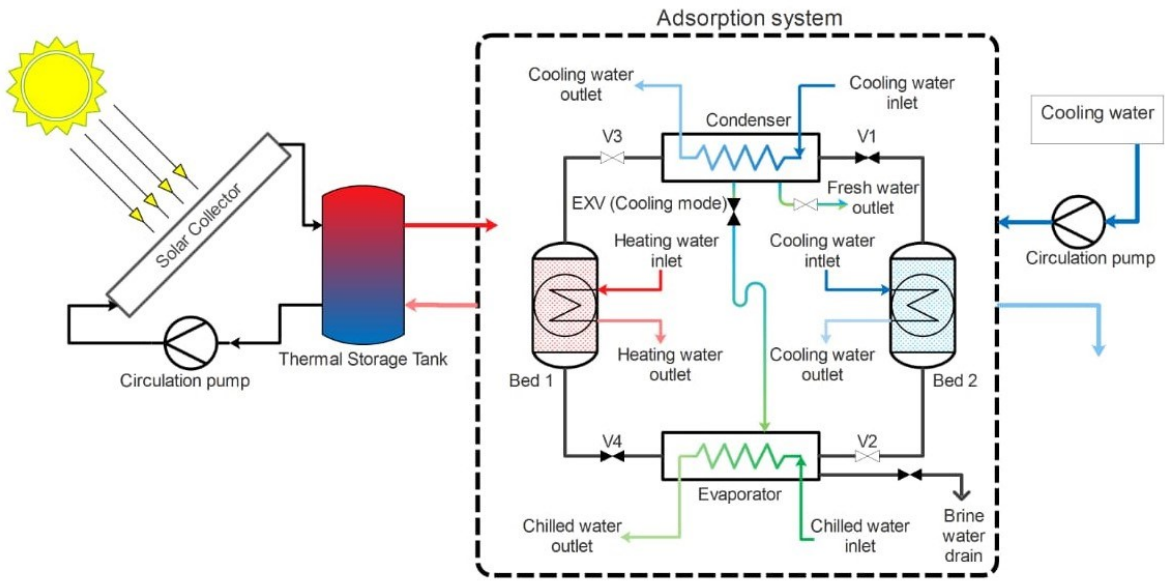

Fig. 1. Schematic diagram of complete system during one operation mode.

Table 1. *Operational and geometric parameters for basic adsorption system used in simulation.*

Parameter	Value	SI
Sorption bed		
No. of modules	7	(−)
Length of module	1	m
Pipe diameter	9.525×10^{-3}	m
Fin height	28×10^{-3}	m
Fin thickness	0.2×10^{-3}	m
No. of tubes/module	25	(−)
No. of passes/tube	1	(−)
Pipe roughness	0.0000015	m
Bed tube thickness	0.8×10^{-3}	m
Cooling water mass flow rate	3.71	kg/s
Cooling water inlet temperature	303	K
Heating water mass flow rate	1.68	kg/s
Condenser		
Total surface area	10.916	m²
Tube diameter	0.0127	m
Tube thickness	0.8×10^{-3}	m
Pipe roughness	0.0000015	m
Cooling water mass flow rate	3.71	kg/s
Cooling water inlet temperature	303	K
Evaporator		
Total surface area	4.9	m²
Tube inner diameter	9×10^{-3}	m
Tube outer diameter	10×10^{-3}	m
Pipe roughness	0.0000015	m
Chilled water mass flow rate	0.9	kg/s

Table 2. Operational and geometric parameters for solar heating system used in simulation.

Parameter	Value	SI unit
Storage tank		
Diameter	0.86	m
Height	1.72	m
Storage tank initial temperature	343	K
Solar collectors		
No. in parallel	9	$(-)$
No. in series	3	$(-)$
Collector inclination angle	45	degree
Ground reflectance	0.2	$(-)$
Mean beam radiation factor	1.13	$(-)$
Piping system of heating water circuit		
Length	100	m
Pipe inner diameter	16×10^{-3}	m
Pipe thickness	5×10^{-3}	m
Insulation thickness	15×10^{-3}	m
Pipe thermal conductivity	0.24	$\mathrm{W/(m.K)}$
Insulation thermal conductivity	0.034	$\mathrm{W/(m.K)}$

3 Computational modeling

3.1 Adsorption subsystem

The adsorption subsystem consists primarily of three components: evaporator, condenser, and adsorption beds. In the adsorption beds, where the thermophysical reactions of adsorption and desorption occur, the adsorbent material is brought into contact with a heat exchanger to exchange heat with heat transfer fluid (HTF). The adsorption beds are sequentially interconnected to the evaporator during the adsorption (exothermic process) and the condenser during the desorption (endothermic process). Three submodels simulate the heat and mass transfer during the adsorption/evaporation and desorption/condensation process. The empirical lumped analytical model (ELAM) was utilized in this study. It should be noticed that the overall heat transfer coefficients (U) for all heat exchangers were vary and calculated based on a thermal resistance network approach developed and discussed in detail, including the source code, by Rezk [56]. Therefore, the heat transfer conductance terms (UA) were not fixed, unlike that typically used in lumped approach utilized in most solar-driven adsorption modeling in open literature. Eqs. 1–4 govern the dynamic energy and mass transfer for adsorption beds, evaporator, and condenser; two operating flags (∂ & φ) govern the interconnection between the

adsorption beds and the other heat exchanger in the different operating modes. It is noteworthy mentioning that the adsorption system works under vacuum at the given operating temperatures. In practice, the system's vacuum is mechanically broken in order to collect the clean water from the condenser side and feed the makeup water in the evaporator side and the time consumed for this process is negligible in the current study. Also, the cooling power that can be lost due to feeding the system with new saline water is neglected in this study, considering most of the feed can be carried out before running the system, and a heat recovery heat exchanger can be used between the cold brine and the new saline water.

$$[M_{ads}w_{bed}Cp_{ref}(T_{bed})+M_{ads}Cp_{ads}+M_{Hex,bed}Cp_{Hex,bed}]\frac{dT_{bed}}{dt}=\partial.\ M_{ads}\frac{dw_{bed}}{dt}\left[\ h_g(T_{Hex})-h_g(P_{Hex},T_{bed})\right]+M_{ads}\frac{dw_{bed}}{dt}\Delta H_{ads}+\sum_{n=1}^{n=N_{bed}}dUA_{bed,k}\times LMTD_{bed} \quad (1)$$

$$Cp_{ref,l}(T_{evap})M_{ref,evap}+M_{Hex,evap}Cp_{Hex,evap})\frac{dT_{evap}}{dt}=UA_{evap}\times LMTD_{evap}+\partial M_{ads}\frac{dw_{bed}}{dt}\left[(h_{ref,evap,l}-h_{ref,evap,g})+Cp_{ads}(T_{cond}-T_{evap})\right] \quad (2)$$

$$Cp_{ref,l}(T_{cond})M_{ref,cond}+M_{Hex,cond}Cp_{Hex,cond})\frac{dT_{cond}}{dt}=UA_{cond}\times LMTD_{cond}+\partial M_{ads}\frac{dw_{bed}}{dt}\left[(h_{ref,cond,l}-h_{ref,cond,g})+Cp_{ads}(T_{cond}-T_{bed})\right] \quad (3)$$

$$\frac{dM_{ref,f,evap}}{dt}=-\ \varphi.\ M_{ads}\left(\frac{dw_{des}}{dt}+\frac{dw_{ads}}{dt}\right) \quad (4)$$

The processes of adsorption and desorption are governed by adsorption kinetics and isotherms. The adsorption kinetics characterize the rate at which the physical reactions of adsorption and desorption occur. The linear driving force (LDF) model is widely used and accepted for governing the adsorption kinetics for working pairs in the absence of interparticle mass transfer resistance.

$$\frac{\partial w}{\partial t}=15\ \frac{D_s}{R_P^2}(W-w) \quad (5)$$

$$K_S a_v=15\ \frac{D_s}{R_P^2} \quad (6)$$

$$D_s=D_{so}\ \exp\left(-\frac{E_a}{Ru\ T}\right) \quad (7)$$

The adsorption isotherm model quantifies the amount of adsorbed adsorbate under equilibrium at given operating temperatures in the adsorbent bed and the interconnected evaporator/condenser. Fig. 2 shows the experimental adsorption isotherms that were investigated: RD SG and Al-Fum. The SG/water adsorption isotherm is classified as type I and best described by the modified Freundlich model shown in Eqs. 8–10 [57].

$$W=A(T_S)\left[\frac{P_s(T_w)}{P_s(T_s)}\right]^{B(T_s)} \quad (8)$$

$$A(T_S)=A_O+A_1T_S+A_2T_S^2+A_3T_S^3 \quad (9)$$

$$B(T_S)=B_O+B_1T_S+B_2T_S^2+B_3T_S^3 \quad (10)$$

The Al-Fum /water pair was modeled using polynomial and exponential equations that were initially reported by Eman et al. [41] and are shown in Eqs. 11–14.

$$C = RT_S\, ln\left(\frac{P_s(T_w)}{P_s(T_s)}\right) \quad (11)$$

$$W = \begin{cases} 0.111993\, exp(-0.000258797\, C) & \text{If } C > 3987 \quad (12) \\ 2.36129 - 9.93768\times10^{-4}\, C + 1.05709\times10^{-7}\, C^2 & \text{If } 2900 \le C \le 3987 \quad (13) \\ 0.5948 - 3.12\times10^{-4}\, C + 1.68302\times10^{-4}\, C^2 - 3.124455\times10^{-11}\, C^3 & \text{If } C < 2900 \quad (14) \end{cases}$$

The thermophysical properties, constants and parameters used in the adsorption isotherm and kinetic models are listed in Table 3. It is noteworthy highlighting the fact that the thermal diffusivity for Al-Fum is 17.3% lower than that for SG, as the specific heat that reflects the heat storage capacity of Al-Fum is 5.3% higher and thermal conductivity that reflects the steady state heat transmissivity is 34.3% lower that these for SG. The low thermal diffusivity of Al-Fum negatively affects the rate of heat transfer at the material level, particularly if operates under unsteady heat sources.

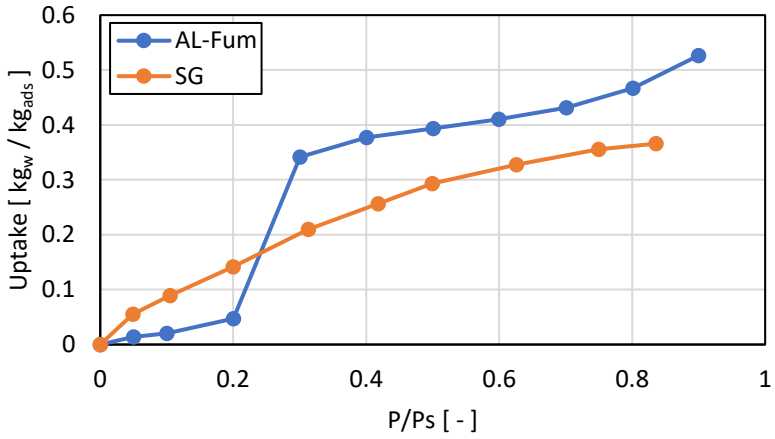

Fig. 2 The experimental isotherms for RD silica gel and aluminum fumarate

Table 3. Thermophysical properties, constants, and parameters of adsorption kinetic and isotherm models.

Adsorption kinetics			
Parameter	SG	Al-Fum	Unit
Dso	2.54×10^{-4}	3.63×10^{-14}	m^2/s
Ea	42000	18026	J/mol
Rp	0.16×10^{-3}	0.65×10^{-6}	m
Adsorption isotherms			
Constant	Value	Constant	Value
A0	−6.5314	B0	−15.587
A1	0.72452×10^{-1}	B1	0.15915
A2	-0.23951×10^{-3}	B2	-0.50612×10^{-3}
A3	0.25493×10^{-6}	B3	0.53290×10^{-6}

Thermophysical properties			
Property	SG	Al-Fum	Unit
Thermal conductivity K	0.198	0.13	$W/(m.K)$
Specific heat C	921	970	$J/(kg.K)$
Thermal diffusivity α	311.6×10^{-9}	257.7×10^{-9}	m^2/s

3.2 Solar collector

Fig. 3 presents the layout of the simulated evacuated tube solar heating system; each unit consists of 15 single-walled glass evacuated tubes. Eq. 15 is a performance equation calculating the thermal efficiency of a single collector [58]. Therefore, each collector outlet temperature $T^{i}_{col,out}$ can be derived from the energy balance on the collector, as given in Eq. 16 . The solar radiation on the tilted surface I_t can be calculated from Eq. 17 based on the solar parameters adopted from Carrier HAP 4.90 for the case under study.

$$\eta^{i}_{col} = a_0 - a_1 \frac{\left(T^{i}_{col,in} - T_{amb}\right)}{I_t} - a_2 \frac{\left(T^{i}_{col,in} - T_{amb}\right)^2}{I_t} \quad (15)$$

$$T^{i}_{col,out} = T^{i}_{col,in} + \frac{\eta^{i}_{col} * A_{sc} * I_t}{m_{col} * C_p} \quad (16)$$

$$I_t = R_{bm}.I_b + I_d.\left(\frac{1+\cos(\beta)}{2}\right) + (I_b + I_d).\rho.\left(\frac{1-\cos(\beta)}{2}\right) \quad (17)$$

where $T^{i}_{col,in}$ stands for the inlet water temperature of a solar collector, T_{amb} is the ambient temperature, A_{sc} is the solar collector effective area, m_{col} is the water mass flow rate through each parallel path, and the superscript i is the order of the collector solved for in series (from 1 to 3). The next collector inlet temperature in the series $T^{i}_{col,in}$ is $T^{i-1}_{col,out}$, and so on. This approach considers the effect of the number of collectors in series on the solar field's overall energy efficiency [59]. The efficiency parameters a_0, a_1, and a_2 were given by the manufacturer for the collector type scm15-58/1800-01 and set as 0.735, 1.349, and 0.015, respectively.

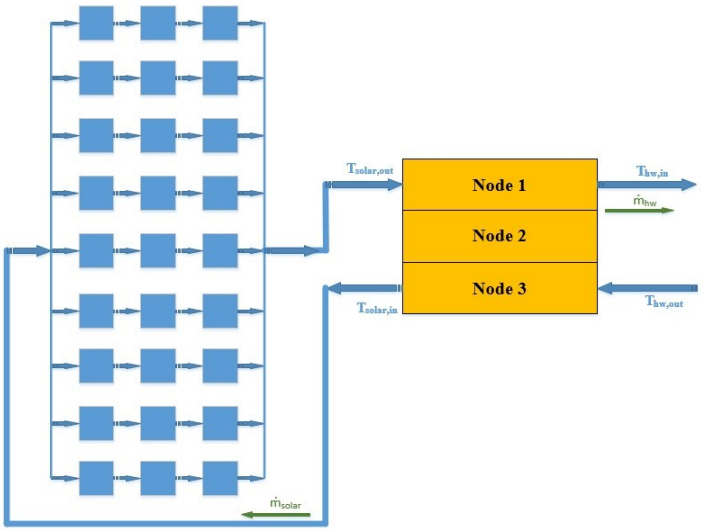

Fig. 3. Schematic diagram of solar heating system modeling approach.

3.3 Thermal energy storage

The hot water thermal energy storage was treated as a one-dimensional stratified tank with three zones: high-temperature zone (T_{s1}), intermediate-temperature zone (T_{s2}), and low-temperature zone (T_{s3})[60]. The volume in the tank was set as 0.5 m^3, and the stored water mass in each zone (M_{HS}) was one-third of the total tank mass. The heat loss from the storage walls to the surroundings was quantified using the estimated heat loss coefficient U_L of 0.5 W/m^2K. Eqs. 18–20 present the energy balance for each zone.

$$M_{HS}c_p\frac{dT_{S1}}{dt} = \dot{m_{solar}}c_p(T_{solar,out} - T_{S1}) + \dot{m}_{hw}\,c_p(T_{S2} - T_{hw,in}) - U_L A_S(T_{S1} - T_{amb}) \quad (18)$$

$$M_{HS}c_p\frac{dT_{S2}}{dt} = \dot{m_{solar}}c_p(T_{S1} - T_{S2}) + \dot{m_{hw}}\,c_p(T_{S3} - T_{S2}) - U_L A_S(T_{S2} - T_{amb}) \quad (19)$$

$$M_{HS}c_p\frac{dT_{S3}}{dt} = \dot{m_{solar}}c_p(T_{S2} - T_{solar,in}) + \dot{m}_{hw}\,c_p(T_{hw,out} - T_{S3}) - U_L A_S(T_{S3} - T_{amb}) \quad (20)$$

In the above equations, A_s is the surface area of the cylindrical storage tank for each zone, and $\dot{m}_{hw}$ is the heating water mass flow rate coming/back from/to the adsorption system.

3.4 Performance indicators

Two performance indicators were used to assess the cyclic performance of the adsorption unit for cooling, namely, the coefficient of performance (COP_{ads}) and specific cooling capacity (SCP_{ads}), as shown in Eqs. 21–22. The overall coefficient of performance (COP_{solar}) at the integrated-system level considering the energy transformation from the total number of solar collectors (N_{sc}) into the cooling power was determined using Eq. 23. The specific daily water production ($SDWP$), determined from Eq. 24, was used to measure the accumulated condensate of pure water drawn from the condenser of the adsorption system for a number of cycles (τ), taken from daylight hours, per the total amount of

adsorbent material (2 .M_{ads}) packed in the two beds. Generally, the COP is a key energy conversion efficiency indicator that assesses system throughput with respect to the energy input.

$$SCP_{ads}=\frac{\int_0^{t_{cycle}} \dot{m}_{chw} C_{P_{chw}} (T_{chw,in}-T_{chw,out}) dt}{t_{cycle}(2 \cdot M_{ads})} \quad (21)$$

$$COP_{ads}=\frac{\int_0^{t_{cycle}} \dot{m}_{chw} C_{P_{chw}} (T_{chw,in}-T_{chw,out}) dt}{\int_0^{t_{cycle}} \dot{m}_{hw} C_{P_{hw}} (T_{hw,in}-T_{hw,out}) dt} \quad (22)$$

$$COP_{solar} = \frac{\int_0^{t_{cycle}} \dot{m}_{chw} C_{P_{chw}} (T_{chw,in}-T_{chw,out}) dt}{\int_0^{t_{cycle}} N_{sc} A_{sc} I_t dt} \quad (23)$$

$$SDWP = \sum_1^{\tau} \int_0^{t_{cycle}} \frac{\dot{m}_{cw} C_{P_{cw}} (T_{cw,in} - T_{cw,out})}{h_{fg} .(2 \cdot M_{ads})} dt \quad (24)$$

4 Numerical method and validation

A MATLAB code was developed in this study to solve numerically and instantaneously the set of equations that previously introduced coupled with the meteorological data of the case under the study using incremental time stepping of 10 s. The thermophysical properties of the adsorbate (water vapor) were continuously updated using REFPROP at each newly calculated temperature and pressure in each subsystem component.

The validation of the adsorption system modeling was already examined in published works and more details about that can be accessible in [38, 39, 56]. For further justification, the validation of the adsorption system modeling has been confirmed using experimental results of aluminum fumarate packed-bed introduced in a reference [48]. Very good agreements have been obtained between the results of the present numerical model in terms of SCP and SDWP with the experimental ones as shown in Fig. 4. At the adsorption bed inlet cooling water temperature of 30 °C, the deviations are -2.25% and 10.65% in the SCP and SDWP, respectively. The solar collector efficiency parameters given by the manufacturer's catalog have been verified by comparing the results of the collector efficiency calculated from Equation 15 with that experimentally calculated from the same test rig pointed out by Elsheniti et al. [59] for a single collector. An acceptable deviation that did not exceed ± 10 % was reported between the present model and experimental results.

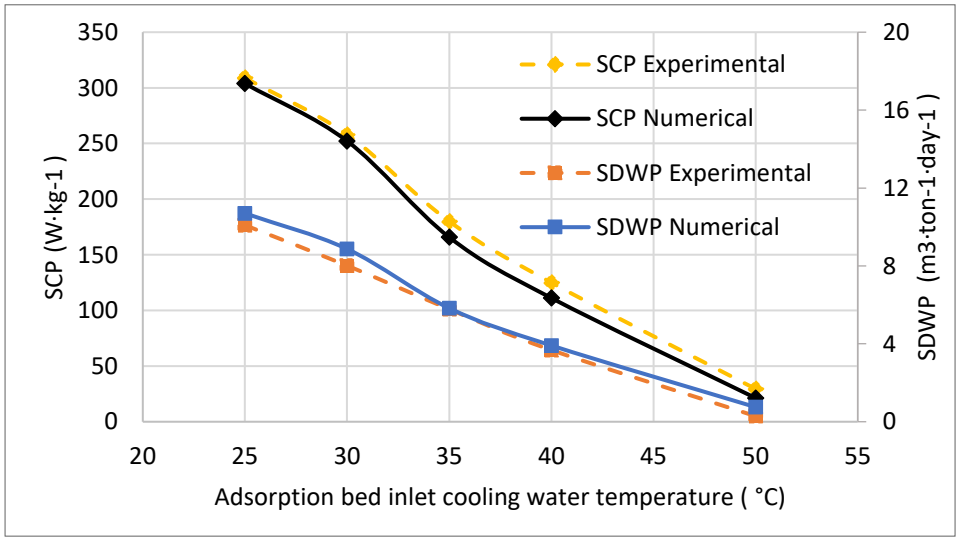

Fig. 4. Validation of the present adsorption numerical model results with experimental results.

5 Results and discussion

5.1 Meteorological data

The heat generated by the solar irradiation and the ambient temperature were determined based on the meteorological data for Alexandria, Egypt, in July between 08:00 and 16:00. The data were coupled with the integrated system to predict system performance throughout the day. The meteorological data displayed in Fig. 5. The mid-day data of each month from April to October were considered in representing the entire month in the simulation.

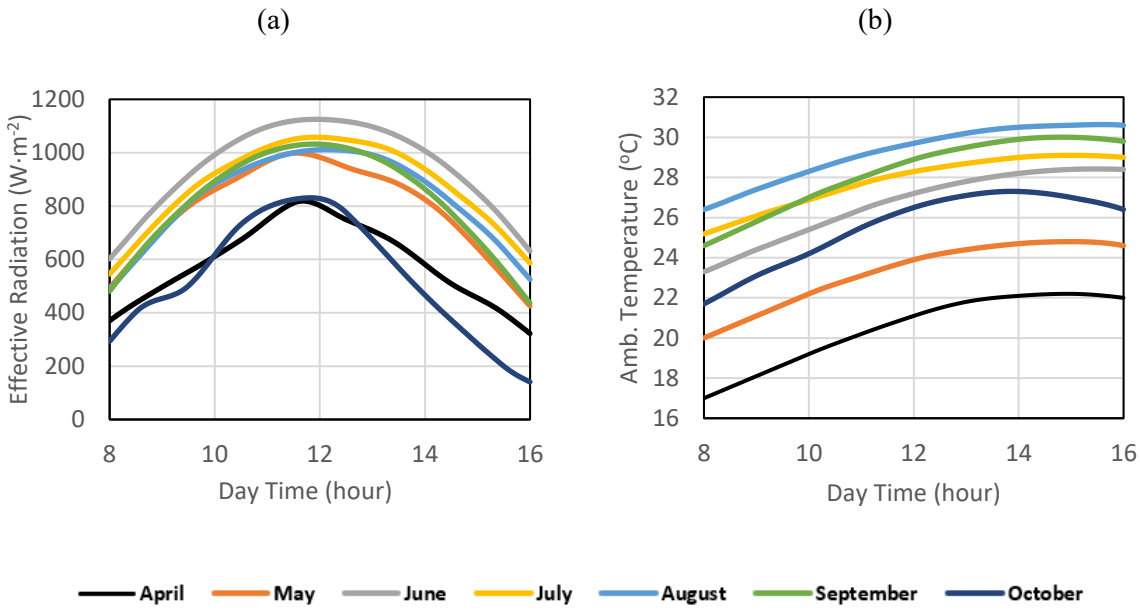

Fig. 5 Meteorological data of Alexandria, Egypt, on mid-days from April to October: a) effective radiation on tilted surface, b) ambient temperature.

5.2 Effect of cycle time

The longer the adsorption process, the more water is adsorbed but the slower the rate of adsorption under near-saturation conditions. Therefore, the effect of cycle time on the system performance and energy conversion efficiency at chilled water inlet temperatures of 15 °C, 20 °C, and 25 °C was investigated. The cycle time for the SG-based system varied from 300 to 800 s, whereas the cycle time varied from 500 to 1000 s in the case of the AF-based system. At cycle times below 500 s, the AF-based system did not perform sufficiently in comparison with the SG-based system; this agrees with previous experimental work [48, 61].

An increase in the chilled water inlet temperature increased the specific cooling power (SCP), SWDP, COP, and COP_{solar}; this primarily resulted from the high cyclic water vapor uptake at higher evaporative temperatures at the material level for both the SG and Al-Fum. The influence of changes in the chilled water temperature on the SCP, SDWP, COP, and COP_{solar} of the AF-based system was more significant than that in the SG-based system over the investigated range of cycle times. Each 5 °C change in the chilled water temperature at a cycle time of 600 s increased the SCP by approximately 49.7 $W \cdot kg^{-1}$ (17.7 $W \cdot kg^{-1}$) and the SDWP by around 0.58 $m^3 \cdot ton^{-1} \cdot day^{-1}$ (0.2 $m^3 \cdot ton^{-1} \cdot day^{-1}$) in the AF-based (SG-based) system, as shown in Fig. 6 and Fig. 7. This resulted from the step change in the AF isotherms at a relative pressure above 0.3, which increased the effective amount of adsorbate in each cycle between the adsorption and desorption modes. The Al-Fum isotherms exhibited typical type IV isotherm behavior (according to IUPAC classification), whereas the SG isotherms were type I isotherms, which follows a gradually increases in water vapor uptake within the operating range [57].

Within the investigated range, the SCP and SDWP increased gradually with the change in cycle time but remain unchanged above 600 s for both systems and the changes did not exceed 1.8%. At the 15 °C chilled water inlet temperature, the COP increased gradually from 0.48 to 0.64 (from 0.36 to 0.48) as the cycle time changed from 300 to 800 s (from 500 s to 1000 s) in the SG-based (AF-based) system, as shown in Fig. 8. COP_{solar} increased gradually from 0.28 to 0.33 (from 0.146 to 0.153) as the cycle time changed from 300 to 600 s (from 500 to 600 s) in the SG-based (AF-based) system, as shown in Fig. 9. Above 600 s, the change in COP_{solar} did not exceed 0.8%. However, the AF-based system required a longer cycle time to sustain the competitiveness of its cycle COP values as an impact of the relatively lower thermal diffusivity of AF at material level that suppress its response. Therefore, the cycle times of 600 s for the SG-based system and 900 s for the AF-based system were selected to determine system performance in the following sections.

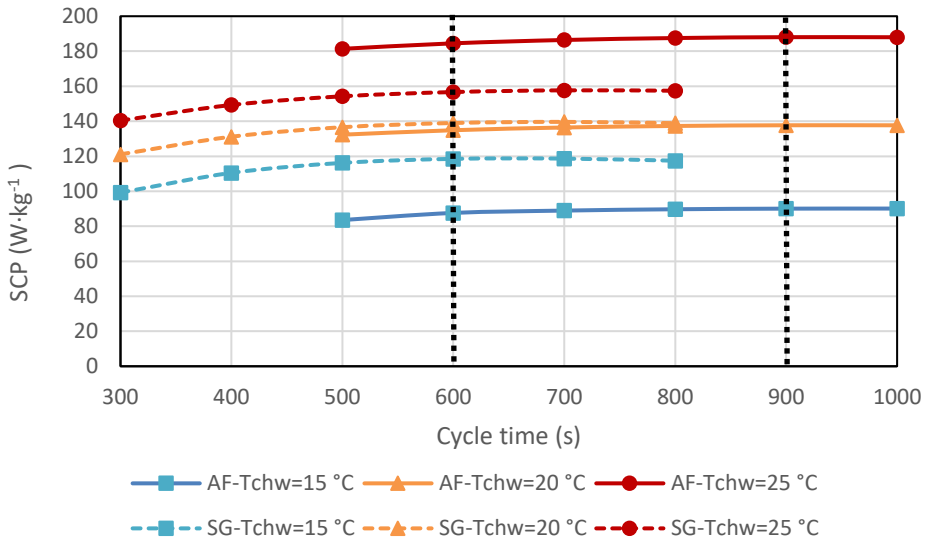

Fig. 6. Effect of cycle time on specific cooling power at different chilled water inlet temperatures.

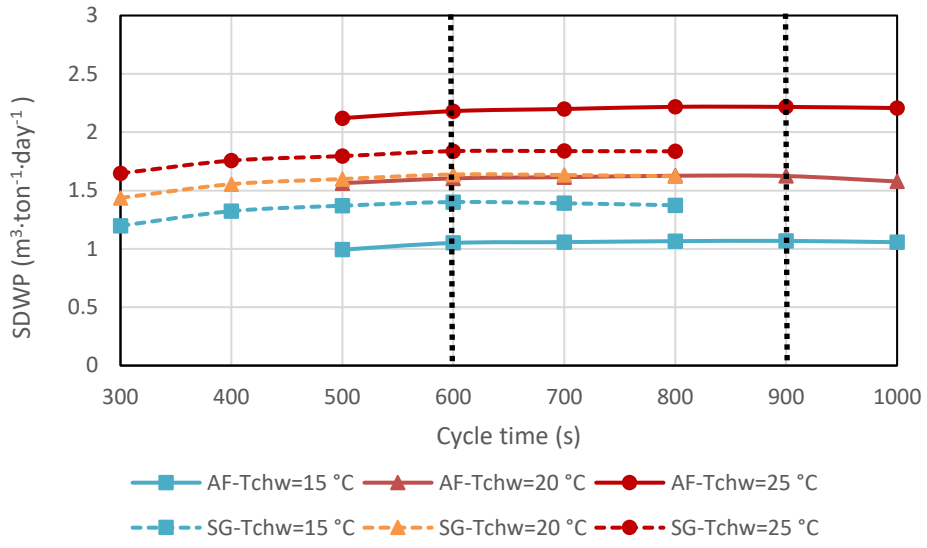

Fig. 7. Effect of cycle time on specific daily water production at different chilled water inlet temperatures.

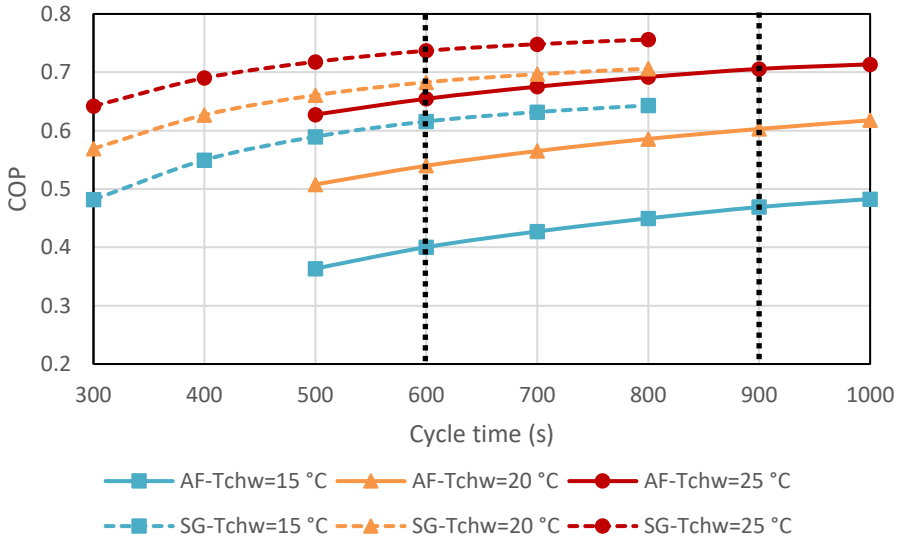

Fig. 8. Effect of cycle time on adsorption system COP at different chilled water inlet temperatures.

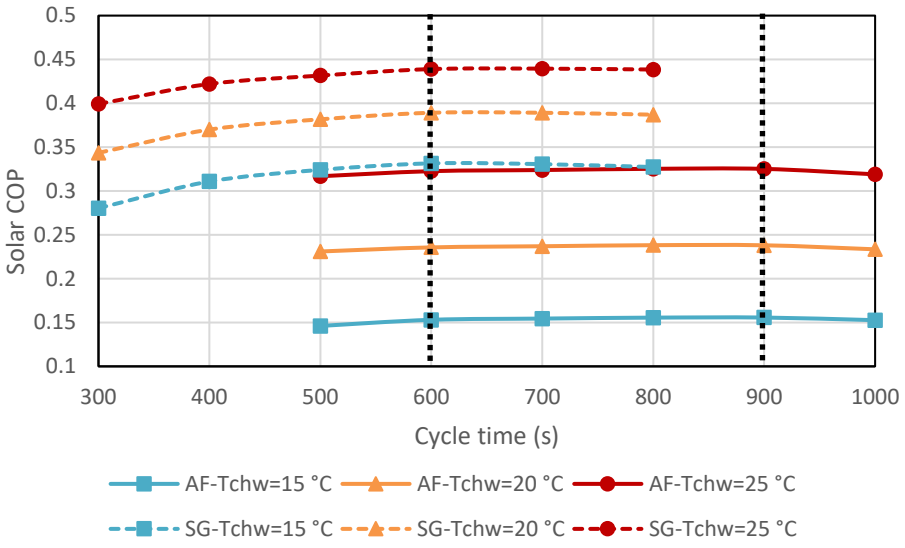

Fig. 9. Effect of cycle time on integrated-system solar COP at different chilled water inlet temperatures.

5.3 Hourly temperature variations

Fig. 10 and Fig. 11 show the hourly variations of all inlet and outlet temperatures for both adsorption cycles during the mid-days of July at the $T_{chw,in}$ of 15 °C to understand the accumulating effect of the heat generated by the solar system on both the SG and Al-Fum adsorption systems. Although the solar heating system and geometric adsorption system parameters were identical for both systems, the circulating heating water in the AF-based system reached higher temperatures and peaked at about 120 °C at 14:00, whereas the maximum temperature of the SG-based system was 87 °C at 13:30. This is attributed to the higher heat stored in each cycle of the AF-based system due to its low thermal diffusivity, coupled with the decreasing in the desorbed amount in each following cycle, under the given condition. Accordingly, the higher the working water temperature, the lower the thermal efficiency of a solar heating system. Consequently, the COP_{solar} of the AF-based system was negatively affected in this case.

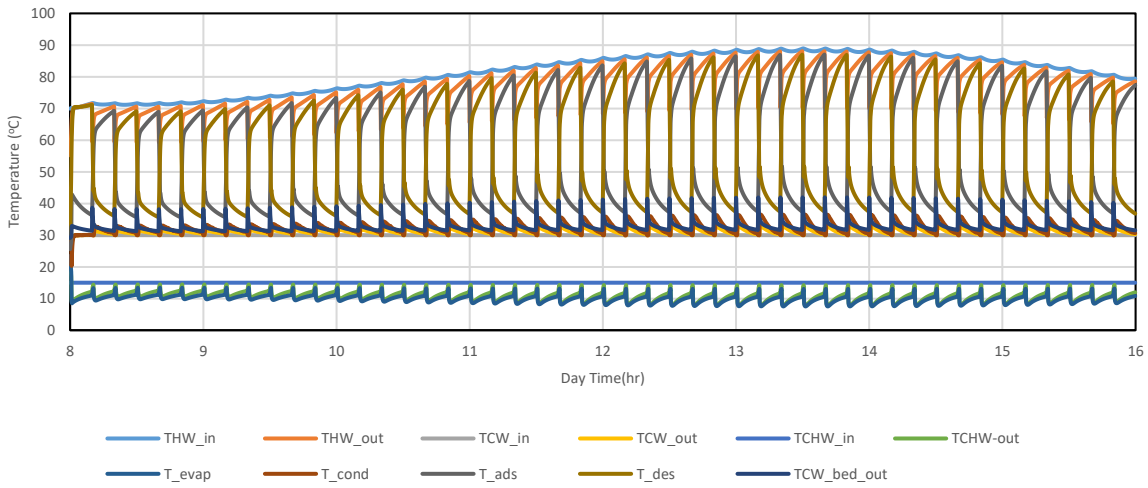

Fig. 10. Hourly temperature variations of SG-based adsorption system at chilled water inlet temperature of 15 °C.

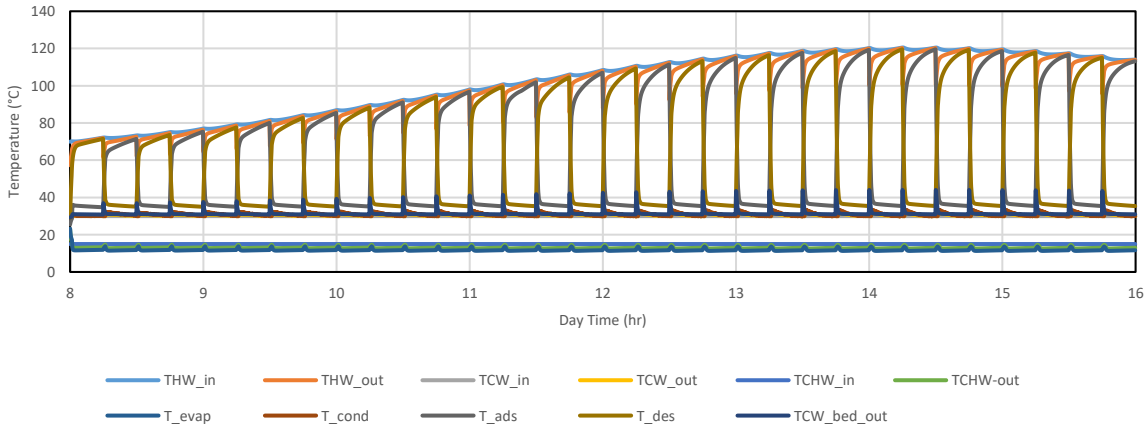

Fig. 11. Hourly temperature variations of AF-based adsorption cycle at chilled water inlet temperature of 15 °C.

5.4 Effect of fin spacing

Adsorbent materials have low thermal conductivity, primarily due to the high porosity of their structures. Conventionally, metallic fins with high thermal diffusivity are used to boost the heat transfer rate in the adsorbent domain within a packed bed of an adsorption system. However, this increases the heat energy required to heat up and cool down such beds. Therefore, fin parameters, particularly fin spacing, considerably influence the adsorption system performance. Such parameters have been studied for adsorption systems driven by fixed temperature heating sources [30]. In this section, the effects of fin spacing on the performance of both the solar-driven Al-Fum and SG systems are investigated considering the solar flux and ambient temperature in the mid-days (between 8:00 and 16:00) of July. In the next section, the investigation is extended to cover the effect of fin spacing considering data from the cooling season (from April to October) for the case under study.

Fig. 12 shows that the daily average SCP increased noticeably as the fin spacing was reduced from 3 to 0.5 mm for both the AF- and SG-based systems; the AF-based system had a more pronounced enhancement at narrow fin spacing. These enhancements in the SCP of both systems at a small fin spacing are attributed to the improvements in the heat transfer within the adsorbent material domain due to the use of more fins. However, the response of each system depended on their adsorption characteristics. The excessive heat consumed in the AF-based beds decreased the circulated regeneration temperature, thereby improving the performance of the AF-based system by a rate higher than that for the SG-based system. As the fin spacing was reduced from 3 to 0.5 mm, the SCP of the AF-based-system increased by 78% and 51% at the $T_{chw,in}$ of 20 °C and 25 °C, respectively, while the SCP of the SG-based system increased by 38% and 40% at these temperatures. The SCP of the SG-based system outperformed that of the AF-based system within the investigated range of fin spacings at the low $T_{chw,in}$ of 15 °C, but the difference between both systems decreased from 29.3 to 3.7 $W \cdot kg^{-1}$ when the fin spacing was reduced from 3 to 0.5 mm.

The increase in the effective amount of adsorbed/desorbed water at the smaller fin spacing directly resulted in the increase in the daily average SCP as well as the SDWP. Therefore, Fig. 13 shows that the change patterns of the SDWP and the daily average SCP caused by the fin spacing were similar; a smaller fin spacing augmented the SDWP for both systems. With the fin spacing changing from 3 to 0.5 mm at the $T_{chw,in}$ of 15 °C, the SDWP of the AF-based system increased by 69%, while that in the SG-based system increased by only 32%. The maximum SDWP reached 3.22 and 2.26 $m^3 \cdot ton^{-1} \cdot day^{-1}$ for the AF- and SG-based systems, respectively, at the high $T_{chw,in}$ of 25 °C.

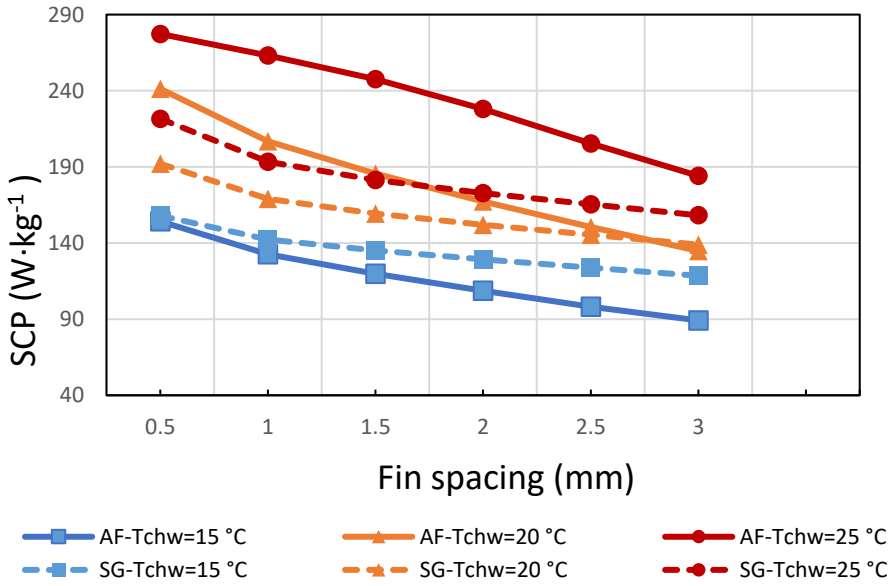

Fig. 12. Effect of fin spacing on SCP at different chilled water temperatures for Al-Fum and SG systems.

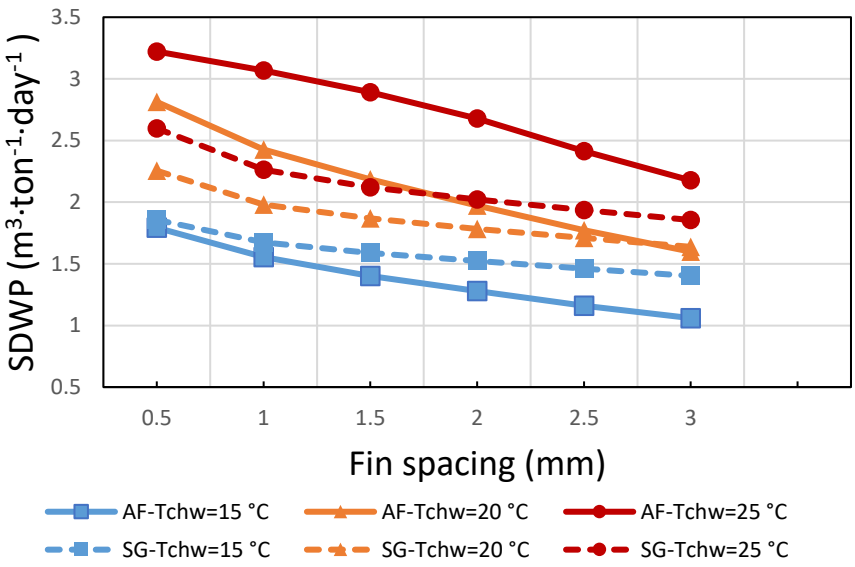

Fig. 13. Effect of fin spacing on SDWP at different chilled water temperatures for Al-Fum and SG systems.

Fig. 14 shows the net effect of the fin spacing on the daily average cycle COP for both adsorption systems. Generally, the adsorption cycle COP of the SG-based system was higher than that of the AF-based system in all investigated cases, but the minimum difference between them was almost eliminated at the best COP of 0.75 for both cycles at the $T_{chw,in}$ of 25 °C and fin spacing of 1.5 mm. An optimum fin spacing of 1–2 mm can be used to obtain the maximum cycle COP at different $T_{chw,in}$ values. Compared with the cycle COP of the SG-based system, that of the AF-based system was more negatively affected by an enlargement in the fin spacing over the optimum one. At the $T_{chw,in}$ of 15 °C, the cycle COP reached its maximum of 0.62 and 0.51 at fin spacings of 2 and 1.5 mm for the SG- and AF-based systems, respectively. Although the best SCPs were attained at the minimum fin spacing of 0.5 mm, the cycle COPs were the lowest in this case. This is attributed to the excessive increase in the thermal mass of the beds as the metal-to-adsorbent ratio increased considerably, leading to higher heat consumed in heating up the adsorbent bed; this negated the positive effect of the SCP increase on the cycle COP.

The daily average solar COP reflects the effect of the overall thermal loss in an integrated system, including the thermal loss in the solar heating system, which is affected by the fin spacing through the temperature of the circulating heating water returning from the adsorption cycle. Fig. 15 shows the net effect of the fin spacing on the average solar COP throughout the day under study. The solar COP of the SG-based system outperformed that of the AF-based system in all the investigated cases, reflecting the increase in heat loss in the AF-based system over that of the SG-based system due to the higher circulating water temperatures in the heating cycle of the former system. The optimum solar COPs, which were almost at fin spacings of 1–1.5 mm for both systems in all cases, were 0.35, 0.42, and 0.48

for the SG-based system and 0.2, 0.31, and 0.4 for the AF-based system at the $T_{chw,in}$ of 15 °C, 20 °C, and 25 °C, respectively.

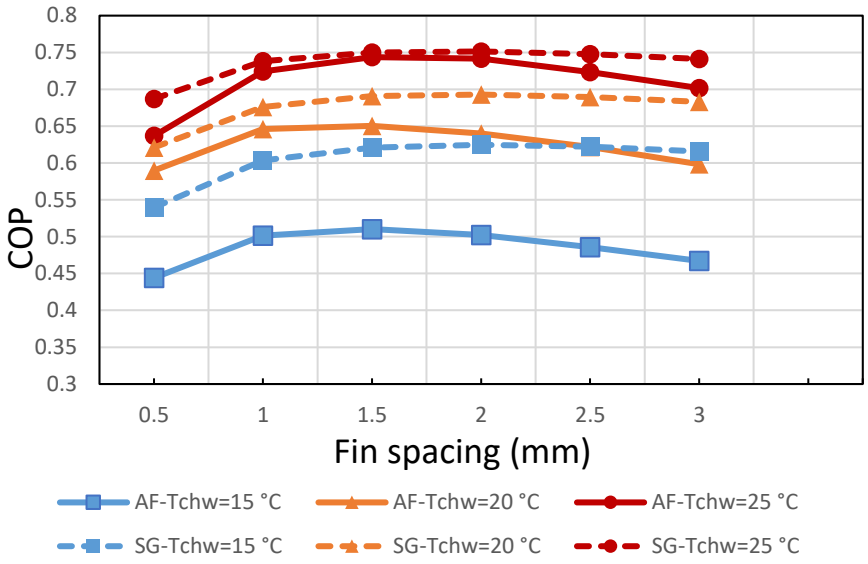

Fig. 14. Effect of fin spacing on COP at different chilled water temperatures for AF and SG systems.

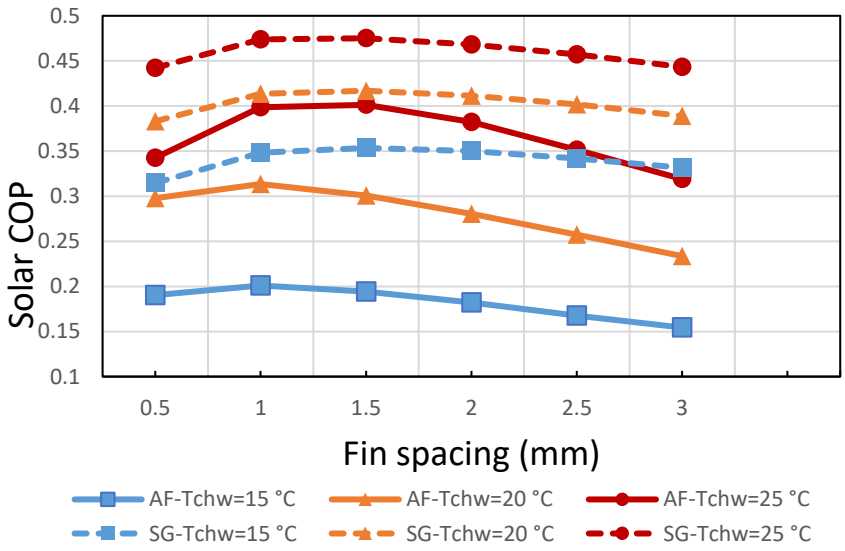

Fig. 15. Effect of fin spacing on solar COP at different chilled water temperatures for Al-Fum and SG systems.

5.5 Monthly system performance

Based on the data in Fig. 5, the net effects of the change in the solar flux and ambient temperature from April to October on the average daily performance of the solar-driven SG and Al-Fum systems are predicted in this section. In addition, fin spacings of 1 and 3 mm are considered in the comparison to explain their net effects in the different months of study.

Fig. 16 shows that the SCPs at the narrow fin spacing of 1 mm were higher than those at the 3 mm fin spacing. The best SCPs for both systems were attained in June owing to the highest effective solar flux in this month; the SCP was as high as 264 $W \cdot kg^{-1}$ for the AF-based system at the $T_{chw,in}$ of 25 °C and the fin spacing of 1 mm. The best SCPs of the AF-based system were higher than those of the SG-based system by −16.6%, 16.8%, and 30.5% at $T_{chw,in}$ of 15 °C, 20 °C, and 25 °C, assuring on the preferences of the AF-based system at a higher $T_{chw,in}$.

At the same $T_{chw,in}$ of 15 °C and 20 °C, The daily average SCPs of the AF-based systems reveal almost constant values for spacing of 3 mm despite of the reduction of the solar flux in April and Oct. Although reducing the spacing to 1 mm reveals lower values in April and Oct., the reduction in case of SG-based systems is much more pronounced, as shown in Fig. 16-a. The daily average SCPs of the SG-based system were in synergy with the variation in the solar flux over the simulated months. This was clear when the SCPs of the AF-based system at $T_{chw,in}$ = 15 °C at the fin spacing of 1 mm were increased by about 36% over those of the SG-based system in April and October. The SCPs of the SG-based system were higher than those of the AF-based system in the rest of the summer months with a higher solar flux. Overall, the SCP of the AF-based system was less negatively affected by the reduction in the solar flux in the case under study.

The SDWP that can be collected from both the Al-Fum and SG systems in the different months at the fin spacings of 1 and 3 mm is displayed in Fig. 17. The SDWP trends were similar to those of the SCP over the various months. The higher the solar flux, the higher the SDWP that can be obtained. This allows the preferences to the SDWP from the AF-based system at higher $T_{chw,in}$. The AF-based system can produce a maximum of 3.1 $m^3 \cdot ton^{-1} \cdot day^{-1}$ in June at the $T_{chw,in}$ of 25 °C and 1 mm fin spacing, which is higher by 30.5% than that of the SG-based system.

Although Al-Fum has a larger effective surface area compared with SG, which enables a higher uptake via an S-shaped isotherm graph, the former's other adsorption characteristics can downplay this advantage. In detail, Al-Fum has a lower activation energy of diffusion (by about one-third) compared with SG. Therefore, Al-Fum is heated up to a temperature higher than that for SG when the same source of heating is used. The higher stored heat during the regeneration process negatively affects the Al-Fum during the adsorption process. In addition, Al-Fum has a far lower pre-exponential constant of surface diffusivity compared with SG, which also slows down the adsorption process for Al-Fum. In a solar-

driven system, the heating source is quadratic, and the loop of the heating fluid is closed. Therefore, the accumulated effects of increasing the temperature of the heating source can further degrade an AF-based system's performance, particularly in summer (as in the case under study). Nonetheless, working under a higher inlet chilled water temperature can considerably increase the amount of uptake, thereby offsetting the negative effects of the lower surface diffusivity. Furthermore, the negative effects of the thermal characteristics of Al-Fum on the integrated system performance were mitigated when a lower heating source was applied.

In applications that require more cooling capacity at lower chilled water temperatures, the $T_{chw,in}$ should be set as 15 °C. The SDWP of an SG-based system will outperform that produced from an AF-based system over most months at both 1 and 3 mm fin spacings.

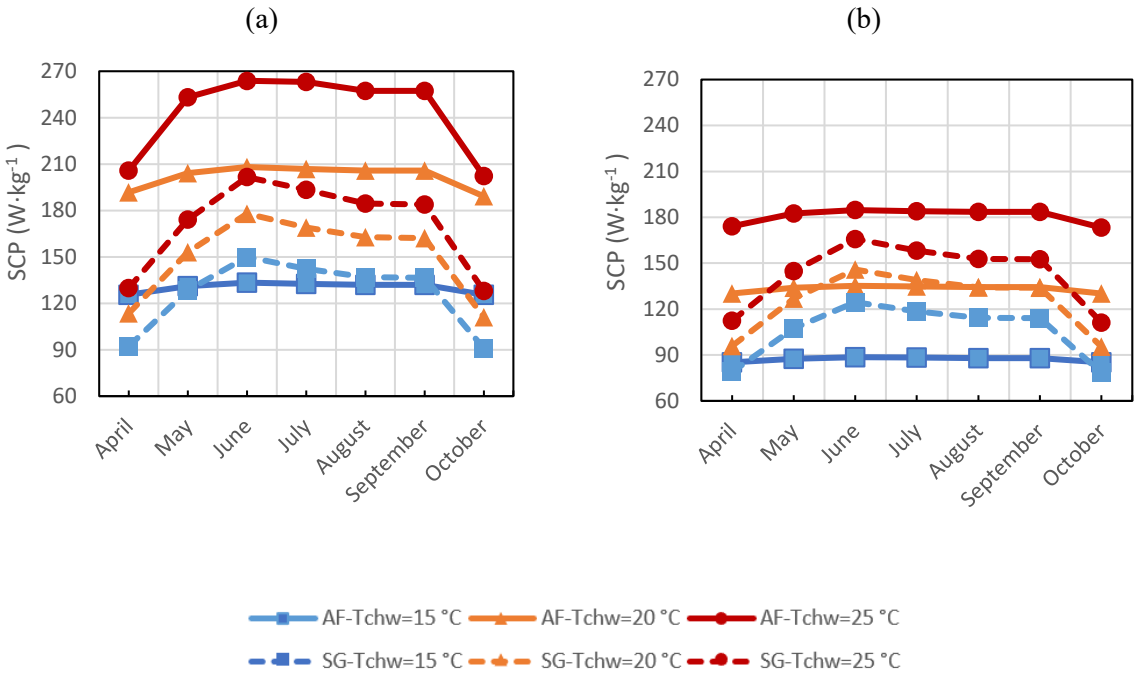

Fig. 16. Average daily SCP over different months at fin spacings of (a) 1 mm and (b) 3 mm.

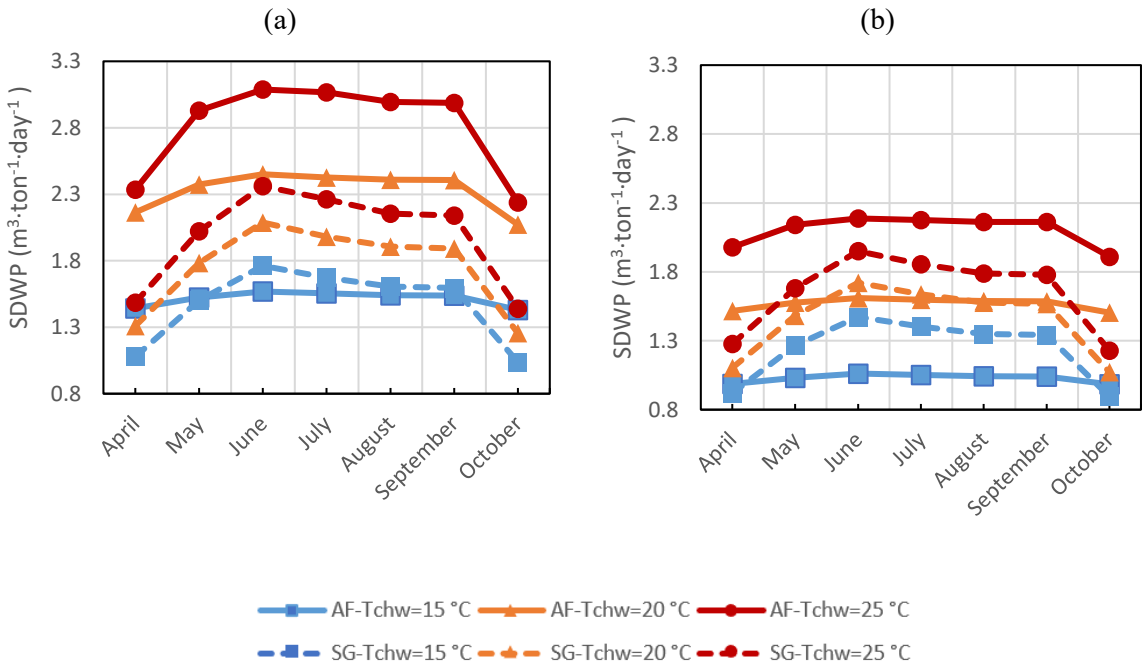

Fig. 17. SDWP over different months at fin spacings of (a) 1 mm and (b) 3 mm.

Fig. 18 shows that the cycle COP of the AF-based system was more positively affected by the reduction in the solar irradiation and the ambient temperature outside the summer season compared with that of the SG-based system at different $T_{chw,in}$ and fin spacings. However, the COPs of the AF-based system outperformed those of the SG-based system in limited cases, particularly in April and October, at higher $T_{chw,in}$ of 20 °C and 25 °C. Otherwise, the SG-based system had higher COPs overall, and they were augmented by 24% and 36% over those of the AF-based system in June at fin spacings of 1 and 3 mm, respectively, at the $T_{chw,in}$ of 15 °C. The COPs of the AF-based system had the lowest values in June (0.49 and 0.45 at these two fin spacings).

The SG-based system had COPs of around 0.6 over the investigated months (April to October) at the $T_{chw,in}$ of 15 °C. However, they increased by approximately 12% and 22% when the $T_{chw,in}$ was 20 °C and 25 °C at the fin spacing of 1 mm. Under the same conditions, the COPs of the AF-based system increased by approximately 29% and 44%.

Regarding the fin spacing's effect on each system over the different months, the SG-based system had a slightly better COP at 3 mm fin spacing. This can be attributed to the effect of the reduction in the bed thermal mass with a smaller fin number, which offset the decrease in the cooling capacity at this wider fin spacing. The COP of the AF-based system was higher at the fin spacing of 1 mm compared with that at the 3 mm fin spacing. This was due to the compensation for the lower thermal conductivity of the AF when the smaller fin spacing was employed, which resulted in an excessive increase in the cooling capacity, thus offsetting the increase in the sensible heat consumed in the preheating and desorption modes.

The trends of the solar COPs of both systems were similar to those of the system COP, as shown in Fig. 19, considering the large reduction in the solar COP related to the AF-based system compared with that related to the SG-based system under the different conditions. Generally, the solar COP of the SG-based system had considerably higher values under the same conditions compared with those of the AF-based system due to the higher heating water temperature in the AF-based system. Consequently, the average solar COPs of the SG-based system over the different months were higher by 83%, 43%, and 22% compared with those of the AF-based system at $T_{chw,in}$ of 15 °C, 20 °C, and 25 °C, respectively, at 1 mm fin spacing. The increase in losses in the heating system over the different months of the AF-bed system was more evident in the summer season, but it was relatively reduced in April and October due to the decrease in the circulating hot water temperature. Moreover, the solar COP of the SG-based system was slightly higher at the fin spacing of 1 mm than that at 3 mm in the different months. The highest solar COP values were achieved in October at different $T_{chw,in}$ for both systems, while the lowest values were obtained in June.

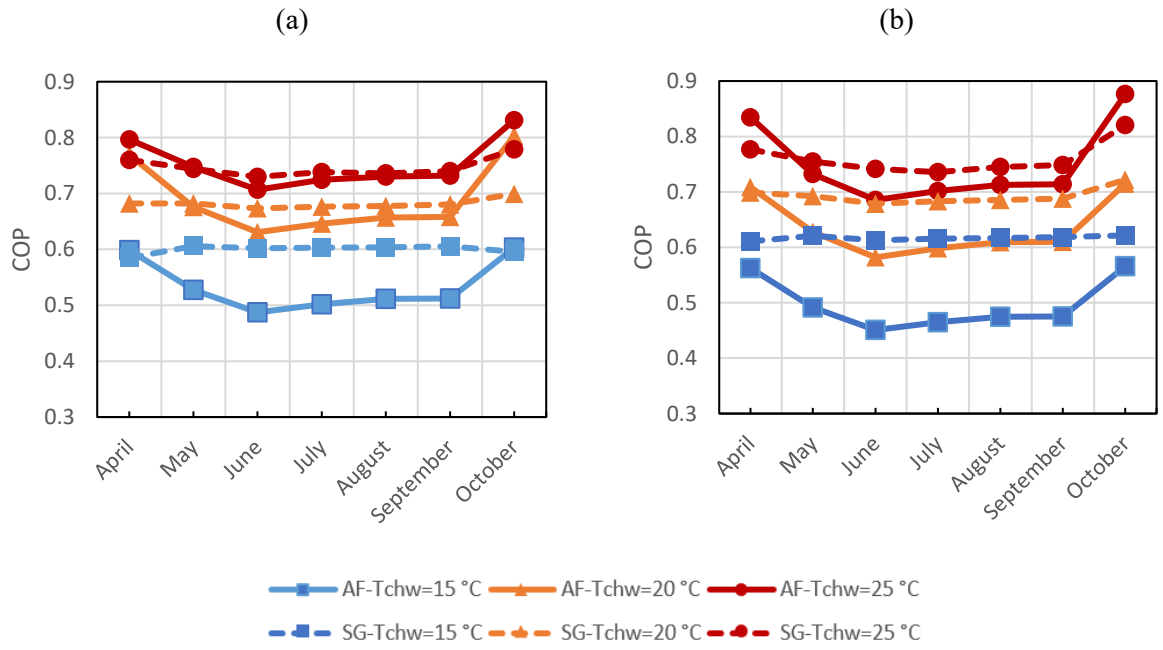

Fig. 18. Adsorption system COP over different months at fin spacings of (a) 1 mm and (b) 3 mm.

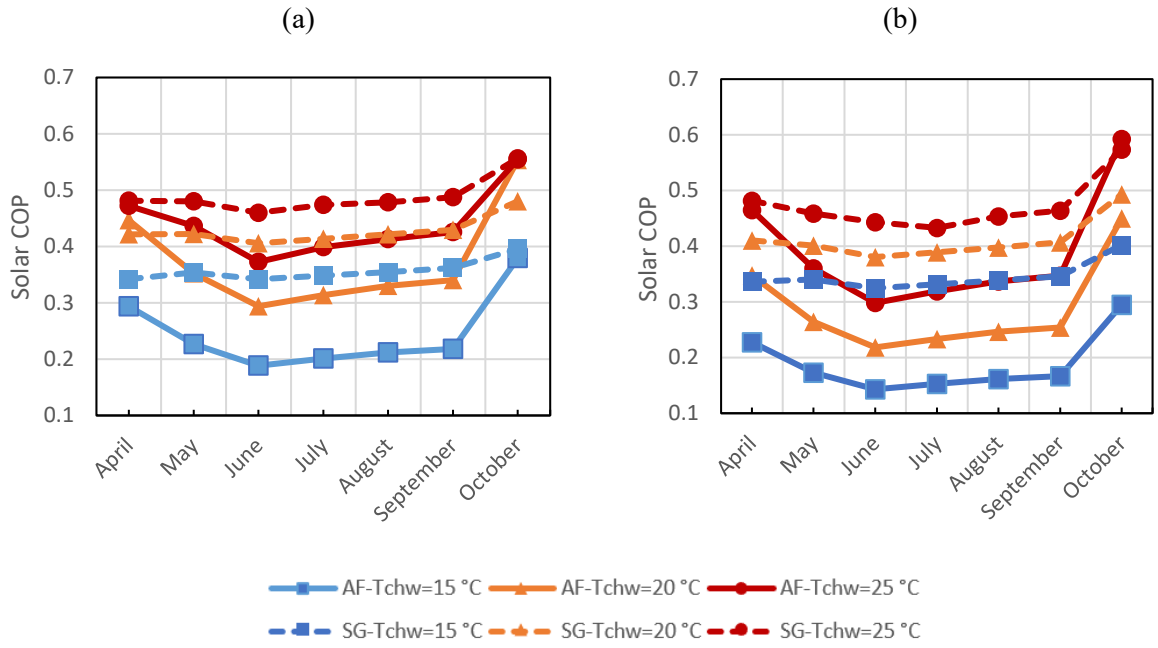

Fig. 19. Solar COP over different months at fin spacings of (a) 1 mm and (b) 3 mm.

5.6 Effect of initial temperature of storage tank

The initial temperature of the storage tank in the preceding sections was fixed at 70 °C at 8:00 for both the AF- and SG-based systems. Decreasing the initial temperature can delay the effective regeneration processes at the early cycles in a day; it will also reduce the daily peak temperatures, hence affecting the energy conversion efficiency of the overall system. Different approaches can be used to determine this temperature theoretically, including continuous simulation over months, to consider the accumulated daily effects of the change in weather and thermal losses. Otherwise, setting 50 °C–70 °C as potential initial temperatures for the hot water tank can give outlines about the performance of both systems under different scenarios. The case considered herein was in the mid-days of July at $T_{chw,in}$ of 15 °C, and adopted the model parameters in Table 1 and fin spacings of 1 and 3 mm.

Fig. 20 shows the percentage changes in the performance parameters of each system at 50 °C and 60 °C initial thermal storage temperatures compared with those at 70 °C. Similar percentage changes can be noticed in each performance parameter when the fin spacing changed from 1 to 3 mm for each system, indicating the clear predominance of the initial temperature on such changes. Startup at temperatures lower than 70 °C for the storage tank can noticeably reduce the performance of the SG-based system, as shown in Fig. 20 a and c, compared with that of the AF-based system, as shown in Fig. 20 b and d. The most affected parameter was the accumulated amount of desalinated water over each day. The SDWP was reduced by about 9.7% and 4.7% (3.8% and 1.1%) for the SG-based (AF-based) system at 50 °C and 60 °C initial temperatures, respectively. The daily average COP of the AF-based (SG-based) system increased by about 0.3% and 1.5% (reduced by 4.1% and 1.6%) at the same initial temperatures

of 50 °C and 60 °C, respectively, at the fin spacing of 1 mm. The daily average SCP of the SG-based (AF-based) system was reduced by 7.5% and 3.6% (2.4% and 0.8%) at the initial temperatures of 50 °C and 60 °C, respectively.

As shown by the absolute values of the performance parameters, the AF-based system's SCP (130 $W \cdot kg^{-1}$) and SDWP (1.5 $m^3 \cdot ton^{-1} \cdot day^{-1}$) were comparable with those of the SG-based system at the low tank initial temperature of 50 °C at 1 mm fin spacing. However, in the same case, the COP and solar COP of the SG-based system noticeably outperformed those of the AF-based system. The COPs and solar COPs of the SG-based system were 0.578 and 0.32, respectively, whereas those of the AF-based system were 0.503 and 0.196, respectively. Therefore, the energy conversion efficiency of the SG-based system was higher than that of the AF-based system by 14.9% in terms of the COP and 63% in terms of the solar COP. At the fin spacing of 3 mm and a low tank initial temperature, the SG-based system performed better than did the AF-based system in all performance parameters. The better COPs for SG-based system owing to its relatively faster response to the cyclic and daily temperature changes due to its higher thermal diffusivity. For example, the SCP of the SG-based system was reduced from 118.5 $W \cdot kg^{-1}$ at 70 °C to 109 $W \cdot kg^{-1}$ at 50 °C, whereas that of the AF-based system decreased from 89.2 $W \cdot kg^{-1}$ at 70 °C to 87.4 $W \cdot kg^{-1}$ at 50 °C.

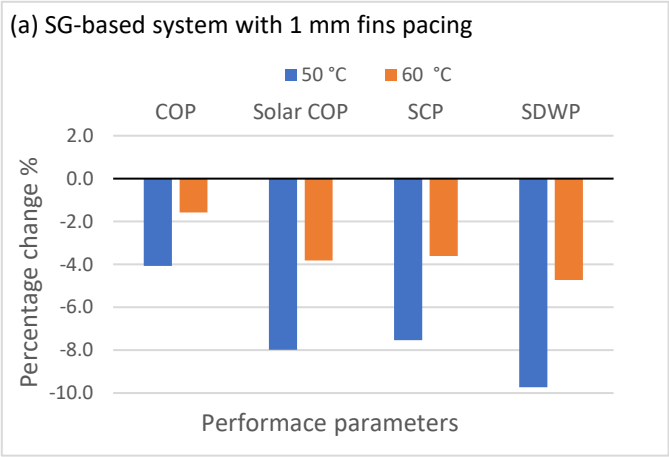

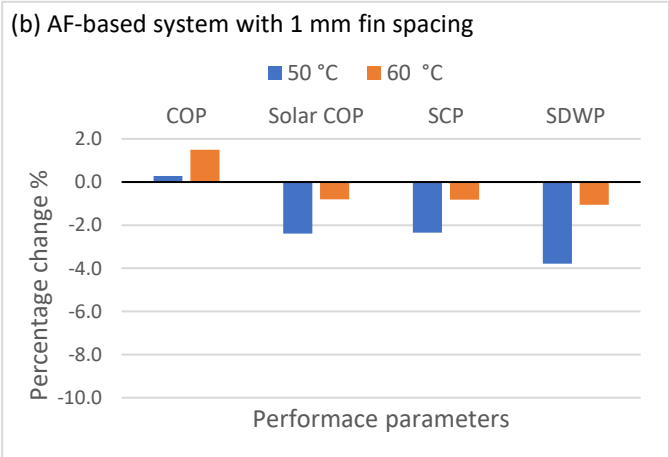

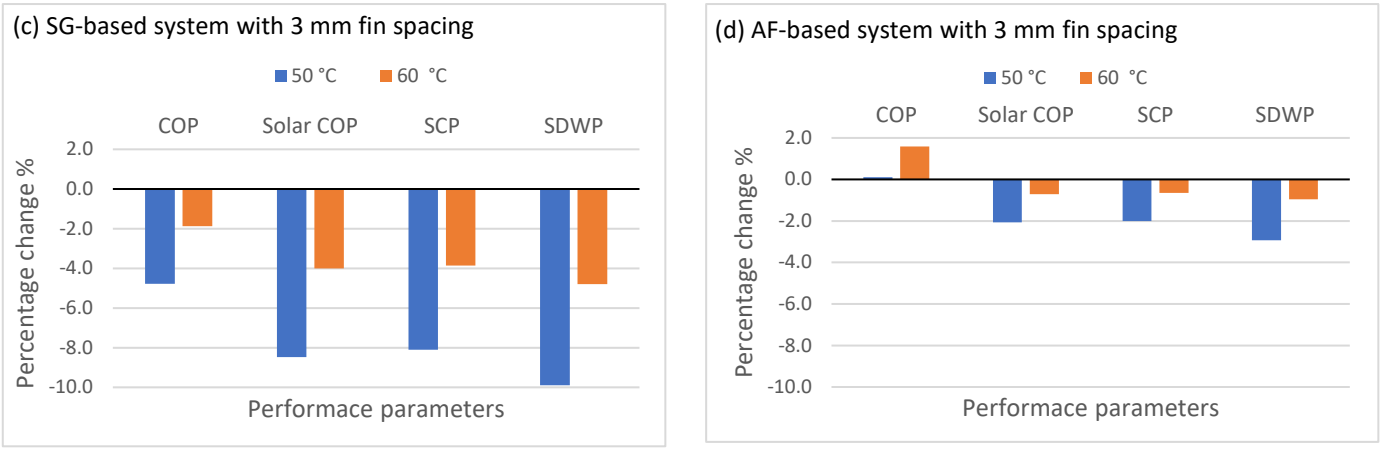

Fig. 20. Effect of initial temperature of water in storage tank on performance parameters of SG and AF systems relative to those at 70 °C and fin spacings of 1 and 3 mm.

6 Conclusions

A comparative investigation was performed on the use of Al-Fum MOF and RD Silica gel in a hybrid adsorption cooling and desalination system, and the main outcomes can be concluded as follows.

- An increase in the chilled water inlet temperature, $T_{chw,in}$, enhanced the SCP, SDWP, COP and COP_{solar} for both systems. This was more significant in the AF-based system due to the step change in the isotherms of Al-Fum.
- The AF-based systems had lower COP and COP_{solar} affected by the lower thermal characteristics of Al-Fum, compared with the SG-based system at almost all investigated cases. As for example, at the highest solar flux, in June, the COPs of the SG-based system were augmented by 24% and 36% over those of the AF-based system that having 0.49 and 0.45 COPs at fin spacings of 1 and 3 mm, respectively.
- Although the best SCPs were attained at the minimum fin spacing of 0.5 mm, the cycle COPs were the lowest in this case affected by the excessive increase in the system thermal mass. Consequently, the COP and COP_{solar} of both systems peaked at 1–2 mm fin spacings.
- The SDWP of the Al-Fum increased by 69% and that was only 32% for SG-based system when fin spacing changed from 3 to 0.5 mm at $T_{chw,in}$ of 15 °C, providing almost the same SDWP.
- The choice of high-performance SCP and SWDP adsorption units at the expenses of the energy conversion efficiency might be evident in the case of renewable heat sources, but poor energy conversion efficiency might lead to large solar panel areas and additional costs of adsorbent materials. These choices are limited in the case of AF-based systems if the chilled water temperature is of concern.
- The SG-based system was more responsive when reducing the initially hot water temperature early in the day from 70 °C to 50 °C, but the COP and COP_{solar} of the SG-based system kept to 14.9%–63% higher than that of the AF-based system.

Acknowledgments

This work was supported by King Saud University, Deanship of Scientific Research, and College of Engineering Research Center.

References

1. Sachs, J., et al., *Clustered spatially and temporally resolved global heat and cooling energy demand in the residential sector.* Applied Energy, 2019. **250**: p. 48-62.
2. Lee, J.-G., K.J. Bae, and O.K. Kwon, *Performance Investigation of a Two-Bed Type Adsorption Chiller with Various Adsorbents.* 2020. **13**(10): p. 2553.
3. Youssef, P.G., R.K. Al-Dadah, and S.M. Mahmoud, *Comparative Analysis of Desalination Technologies.* Energy Procedia, 2014. **61**: p. 2604-2607.
4. Rosales-Asensio, E., et al., *Stress mitigation of conventional water resources in water-scarce areas through the use of renewable energy powered desalination plants: An application to the Canary Islands.* Energy Reports, 2019.
5. Lazzarin, R.M. and M. Noro, *Past, present, future of solar cooling: Technical and economical considerations.* Solar Energy, 2018. **172**: p. 2-13.
6. Noro, M. and R.M. Lazzarin, *Solar cooling between thermal and photovoltaic: An energy and economic comparative study in the Mediterranean conditions.* Energy, 2014. **73**: p. 453-464.
7. Allouhi, A., et al., *Solar driven cooling systems: An updated review.* Renewable and Sustainable Energy Reviews, 2015. **44**: p. 159-181.
8. Aubrée, R., et al., *Design of an efficient small wind-energy conversion system with an adaptive sensorless MPPT strategy.* Renewable Energy, 2016. **86**: p. 280-291.
9. Menale, C., et al., *Thermal management of lithium-ion batteries: An experimental investigation.* Energy, 2019. **182**: p. 57-71.
10. Bataineh, K. and Y. Taamneh, *Review and recent improvements of solar sorption cooling systems.* Energy and Buildings, 2016. **128**: p. 22-37.
11. Zheng, Y. and K.B. Hatzell, *Technoeconomic analysis of solar thermal desalination.* Desalination, 2020. **474**: p. 114168.
12. Behi, M., et al., *Evaluation of a novel solar driven sorption cooling/heating system integrated with PCM storage compartment.* Energy, 2018. **164**: p. 449-464.
13. Alsaman, A.S., et al., *A state of the art of hybrid adsorption desalination–cooling systems.* Renewable and Sustainable Energy Reviews, 2016. **58**: p. 692-703.
14. Thu, K., et al., *A hybrid multi-effect distillation and adsorption cycle.* Applied Energy, 2013. **104**: p. 810-821.
15. Kim, Y.-D., et al., *Water quality assessment of solar-assisted adsorption desalination cycle.* Desalination, 2014. **344**: p. 144-151.
16. Elsheniti, M.B., et al., *Experimental evaluation of a solar two-bed lab-scale adsorption cooling system.* Alexandria Engineering Journal, 2021. **60**(3): p. 2747-2757.
17. Sha, A.A. and V. Baiju, *Thermodynamic analysis and performance evaluation of activated carbon-ethanol two-bed solar adsorption cooling system.* International Journal of Refrigeration, 2021. **123**: p. 81-90.
18. Liu, Y.M., et al., *Evaluation on performance of solar adsorption cooling of silica gel and SAPO-34 zeolite.* Applied Thermal Engineering, 2021. **182**: p. 116019.

19. Rezk, H., et al., *Identifying optimal operating conditions of solar-driven silica gel based adsorption desalination cooling system via modern optimization.* Solar Energy, 2019. **181**: p. 475-489.

20. Logesh, K., et al., *Effect of mass recovery evaporator temperature and condenser temperature on the performance of a solar adsorption-based desalination plant.* International Journal of Ambient Energy, 2017. **40**(2): p. 131-134.

21. Raj, R. and V. Baiju, *Thermodynamic Analysis of a Solar Powered Adsorption Cooling and Desalination System.* Energy Procedia, 2019. **158**: p. 885-891.

22. Du, B., et al., *Area optimization of solar collectors for adsorption desalination.* Solar Energy, 2017. **157**: p. 298-308.

23. Wang, X. and H.T. Chua, *Two bed silica gel–water adsorption chillers: An effectual lumped parameter model.* International Journal of Refrigeration, 2007. **30**(8): p. 1417-1426.

24. Wu, J.Y. and S. Li, *Study on cyclic characteristics of silica gel–water adsorption cooling system driven by variable heat source.* Energy, 2009. **34**(11): p. 1955-1962.

25. Miyazaki, T. and A. Akisawa, *The influence of heat exchanger parameters on the optimum cycle time of adsorption chillers.* Applied Thermal Engineering, 2009. **29**(13): p. 2708-2717.

26. Uyun, A.S., et al., *Numerical analysis of an advanced three-bed mass recovery adsorption refrigeration cycle.* Applied Thermal Engineering, 2009. **29**(14-15): p. 2876-2884.

27. Maggio, G., et al., *Simulation of a solid sorption ice-maker based on the novel composite sorbent "lithium chloride in silica gel pores".* Applied Thermal Engineering, 2009. **29**(8-9): p. 1714-1720.

28. Saha, B.B., et al., *A new generation cooling device employing CaCl2-in-silica gel–water system.* International Journal of Heat and Mass Transfer, 2009. **52**(1-2): p. 516-524.

29. Wang, X. and H.T. Chua, *A comparative evaluation of two different heat-recovery schemes as applied to a two-bed adsorption chiller.* International Journal of Heat and Mass Transfer, 2007. **50**(3): p. 433-443.

30. Elsheniti, M.B., M.A. Hassab, and A.-E. Attia, *Examination of effects of operating and geometric parameters on the performance of a two-bed adsorption chiller.* Applied Thermal Engineering, 2019. **146**: p. 674-687.

31. Albaik, I., et al., *Non-equilibrium numerical modelling of finned tube heat exchanger for adsorption desalination/cooling system using segregated solution approach.* Applied Thermal Engineering, 2021. **183**: p. 116171.

32. Li, M., et al., *Computational fluid dynamic study on adsorption-based desalination and cooling systems with stepwise porosity distribution.* Desalination, 2021. **508**: p. 115048.

33. ul Qadir, N., S.A.M. Said, and R.B. Mansour, *Performance prediction of a two-bed solar adsorption chiller with adaptive cycle time using a MIL-100(Fe)/water working pair – influence of solar collector configuration.* International Journal of Refrigeration, 2018. **85**: p. 472-488.

34. Jafari, A. and A. Haghighi Poshtiri, *Passive solar cooling of single-storey buildings by an adsorption chiller system combined with a solar chimney.* Journal of Cleaner Production, 2017. **141**: p. 662-682.

35. Poshtiri, A.H., S. Bahar, and A. Jafari, *Daily cooling of one-story buildings using domed roof and solar adsorption cooling system.* Applied Energy, 2016. **182**: p. 299-319.

36. Alsaman, A.S., et al., *Performance evaluation of a solar-driven adsorption desalination-cooling system.* Energy, 2017. **128**: p. 196-207.

37. Ali, E.S., et al., *Weather effect on a solar powered hybrid adsorption desalination-cooling system: A case study of Egypt's climate.* Applied Thermal Engineering, 2017. **124**: p. 663-672.

38. Rezk, A., et al., *Effects of contact resistance and metal additives in finned-tube adsorbent beds on the performance of silica gel/water adsorption chiller.* Applied Thermal Engineering, 2013. **53**(2): p. 278-284.

39. Rezk, A.R.M. and R.K. Al-Dadah, *Physical and operating conditions effects on silica gel/water adsorption chiller performance.* Applied Energy, 2012. **89**(1): p. 142-149.

40. Al-Dadah, R., et al., *Metal-organic framework materials for adsorption heat pumps.* Energy, 2019: p. 116356.

41. Elsayed, E., et al., *Aluminium fumarate and CPO-27(Ni) MOFs: Characterization and thermodynamic analysis for adsorption heat pump applications.* Applied Thermal Engineering, 2016. **99**: p. 802-812.

42. Furukawa, H., et al., *The Chemistry and Applications of Metal-Organic Frameworks.* Science, 2013. **341**(6149): p. 1230444.

43. Rezk, A., et al., *Experimental investigation of metal organic frameworks characteristics for water adsorption chillers.* Proceedings of the Institution of Mechanical Engineers, Part C: Journal of Mechanical Engineering Science, 2012. **227**(5): p. 992-1005.

44. Teo, H.W.B. and A. Chakraborty, *Water Adsorption on Various Metal Organic Framework.* IOP Conference Series: Materials Science and Engineering, 2017. **272**: p. 012019.

45. Teo, H.W.B., A. Chakraborty, and S. Kayal, *Formic acid modulated (fam) aluminium fumarate MOF for improved isotherms and kinetics with water adsorption: Cooling/heat pump applications.* Microporous and Mesoporous Materials, 2018. **272**: p. 109-116.

46. Teo, H.W.B., et al., *Experimental study of isotherms and kinetics for adsorption of water on Aluminium Fumarate.* International Journal of Heat and Mass Transfer, 2017. **114**: p. 621-627.

47. Elsayed, E., et al., *CPO-27(Ni), aluminium fumarate and MIL-101(Cr) MOF materials for adsorption water desalination.* Desalination, 2017. **406**: p. 25-36.

48. Elsayed, E., et al., *Experimental testing of aluminium fumarate MOF for adsorption desalination.* Desalination, 2020. **475**: p. 114170.

49. Jahan, I., et al., *Experimental Study on the Influence of Metal Doping on Thermophysical Properties of Porous Aluminum Fumarate.* Heat Transfer Engineering, 2020: p. 1-10.

50. Kummer, H., et al., *A Functional Full-Scale Heat Exchanger Coated with Aluminum Fumarate Metal–Organic Framework for Adsorption Heat Transformation.* Industrial & Engineering Chemistry Research, 2017. **56**(29): p. 8393-8398.

51. Tan, B., et al., *In Situ Synthesis and Performance of Aluminum Fumarate Metal–Organic Framework Monolithic Adsorbent for Water Adsorption.* Industrial & Engineering Chemistry Research, 2019. **58**(34): p. 15712-15720.

52. Saleh, M.M., et al., *Wire fin heat exchanger using aluminium fumarate for adsorption heat pumps.* Applied Thermal Engineering, 2020. **164**: p. 114426.

53. Sharafian, A., et al., *Thermal conductivity and contact resistance of mesoporous silica gel adsorbents bound with polyvinylpyrrolidone in contact with a metallic substrate for adsorption cooling system applications.* International Journal of Heat and Mass Transfer, 2014. **79**: p. 64-71.

54. Huang, B.L., et al., *Thermal conductivity of a metal-organic framework (MOF-5): Part II. Measurement.* International Journal of Heat and Mass Transfer, 2007. **50**(3): p. 405-411.

55. Elsheniti, M.B., et al., *Adsorption Refrigeration Technologies*, in *Sustainable air conditioning systems.* 2018, IntechOpen. p. 71-95.

56. Rezk, A., *Theoretical and experimental investigation of silica gel / water adsorption refrigeration systems*. 2012, University of Birmingham.

57. Saha, B.B., E.C. Boelman, and T. Kashiwagi. *Computer simulation of a silica gel-water adsorption refrigeration cycle - the influence of operating conditions on cooling output and COP*. in *ASHRAE Transactions*. 1995.

58. Kalogirou, S.A., *Solar thermal collectors and applications.* Progress in Energy and Combustion Science, 2004. **30**(3): p. 231-295.

59. Elsheniti, M.B., A. Kotb, and O. Elsamni, *Thermal performance of a heat-pipe evacuated-tube solar collector at high inlet temperatures.* Applied Thermal Engineering, 2019. **154**: p. 315-325.

60. Bellos, E., C. Tzivanidis, and K.A. Antonopoulos, *Exergetic, energetic and financial evaluation of a solar driven absorption cooling system with various collector types.* Applied Thermal Engineering, 2016. **102**: p. 749-759.

61. Al-Dadah, R., et al., *Metal-organic framework materials for adsorption heat pumps.* Energy, 2020. **190**: p. 116356.